**RESEARCH ARTICLE**

# On the Mobility Effect in UAV-Mounted Absorbing Metasurfaces: A Theoretical and Experimental Study

**ALEXANDROS PITILAKIS**[1,2], (Senior Member, IEEE),
**DIMITRIOS TYROVOLAS**[1,3], (Graduate Student Member, IEEE),
**PRODROMOS-VASILEIOS MEKIKIS**[1], (Member, IEEE), **SOTIRIS A. TEGOS**[1], (Member, IEEE),
**ALEXANDROS PAPADOPOULOS**[4], **AGELIKI TSIOLIARIDOU**[2],
**ODYSSEAS TSILIPAKOS**[5], (Senior Member, IEEE), **DIONYSIOS MANESSIS**[6],
**SOTIRIS IOANNIDIS**[2,3], **NIKOLAOS V. KANTARTZIS**[1], (Senior Member, IEEE),
**IAN F. AKYILDIZ**[7], (Life Fellow, IEEE), **AND CHRISTOS K. LIASKOS**[2,4], (Member, IEEE)

[1]School of Electrical and Computer Engineering, Aristotle University of Thessaloniki, 54124 Thessaloniki, Greece
[2]Institute of Computer Science, Foundation for Research and Technology Hellas (FORTH), Heraklion, 70013 Crete, Greece
[3]School of Electrical and Computer Engineering, Technical University of Crete, 73100 Chania, Greece
[4]Computer Science and Engineering Department, University of Ioannina, 45110 Ioannina, Greece
[5]Theoretical and Physical Chemistry Institute, National Hellenic Research Foundation, 11635 Athens, Greece
[6]Department of System Integration and Interconnection Technologies, Fraunhofer IZM, 13355 Berlin, Germany
[7]Truva Inc., Alpharetta, GA 30022, USA

Corresponding author: Alexandros Pitilakis (alexpiti@auth.gr)

**ABSTRACT** In this work, we focus on the theoretical modeling and experimental evaluation of absorbing metasurfaces mounted on unmanned aerial vehicles (UAVs) as facilitators for secure wireless communication channels. Specifically, we present a network architecture based on UAV-mounted metasurfaces and conduct a comprehensive analysis of its components. Furthermore, by utilizing physical optics, namely the Fresnel-Kirchhoff diffraction formula, we develop a comprehensive path loss model that accurately calculates the scattering of wavefronts from metasurfaces with arbitrary configurations; this model enables the quantification of path loss and mobility effects, including pointing accuracy, misalignment, and UAV flying stability, for both near- and far-field conditions. Finally, experimental measurements are conducted using a state-of-the-art static absorbing metasurface and a commercial UAV in an anechoic chamber environment and close agreement between theoretical and experimental results, down to the radiative near-field region, is illustrated. Specifically, our findings indicate that absorbing metasurfaces can act as notch filters with minimal impact on pointing and positioning accuracy, exhibiting a 3 dB beamwidth of $\pm 15°$ compared to ideal static conditions.

**INDEX TERMS** Metasurface, reconfigurable intelligent surface (RIS), unmanned aerial vehicle (UAV), mobility, physical optics, path loss model, diffraction, Fresnel-Kirchhoff.

## I. INTRODUCTION
Metasurfaces are ultrathin artificial structures composed of reflecting and/or refracting elements that are smaller than the

The associate editor coordinating the review of this manuscript and approving it for publication was Zaharias D. Zaharis.

wavelength of the electromagnetic (EM) waves with which they interact [1]. These scattering elements, also known as unit cells, collectively modify incoming waves by redirecting them in specific directions or absorbing them, enabling the metasurface to perform multiple EM functionalities [2]. However, the response of metasurfaces often exhibits significant

spectral and angular dispersion arising from the physical resonances in the unit cells, that may significantly affect the performed functionality. This highlights the crucial importance of meticulous EM design and thorough characterization of metasurfaces for their effective utilization in future wireless networks.

Recently, the extensive utilization of metasurfaces in communication environments presents a paradigm shift by transforming traditionally uncontrollable and stochastic phenomena, such as fading and scattering, into system parameters that can be optimized alongside other variables [3]. In addition to the EM configuration of the metasurface's unit cells, the precise positioning and orientation of the metasurface relative to the source and receiver determine the angle at which EM waves impinge upon and scatter from the metasurface unit cells, influencing the overall system behavior [4]. Therefore, an accurate positioning system is required, being able to adjust the position and orientation of the metasurface to properly align with the incoming and intended outgoing wavefront.

In recent years, the integration of metasurfaces into non-terrestrial networks has been extensively investigated, demonstrating significant enhancements in various aspects of wireless networks [5], [6]. Specifically, the planar geometry of metasurfaces facilitates their integration with unmanned aerial vehicles (UAVs), thus enabling the establishment of deterministic wireless communications based on aerial components. In fact, by taking into account the diverse EM functionalities that can be performed by a metasurface, along with the remarkable versatility of UAVs, it becomes feasible to deploy UAV-mounted metasurfaces strategically and provide distinct metasurface-enabled services, which can be attributed to the favorable characteristics of air-to-ground communication links [7], [8].

### A. RELATED WORK

As previously noted, metasurfaces have the capacity to deliver a variety of EM wavefront-shaping functionalities, including beam steering, beam splitting, and absorption. In this direction, considering the flexibility of UAVs, these metasurfaces can be deployed via UAVs whenever and wherever required to enhance communication performance. For instance, in [9], a UAV-mounted programmable metasurface, reported as UAV-mounted reconfigurable intelligent surface (RIS), was used to meet the stringent demands of ultra-reliable low latency communications via beam steering. Similarly, [10] explored how UAV-mounted RISs can aid mmWave base stations in providing better coverage, while the authors in [11] studied the performance of a solar-powered UAV-mounted RIS that was utilized to establish communication between a base station (BS) and a network user in an energy efficient manner. Furthermore, in the context of internet of things (IoT) networking, [12] proposed a simultaneous wireless power transfer and information transmission scheme for IoT devices with support from a beam-steering

UAV-mounted RIS, while the authors in [13] presented a novel IoT data collection scheme based on UAV-mounted RISs and a novel random access protocol named slotted-ALOHA with code combining. Finally, [14] optimized the average sum of age of information in a UAV-mounted RIS-assisted IoT network. This optimization involved the RIS configuration, the placement of the UAV-mounted RIS, and the scheduling of sensor transmissions, which were achieved through deep reinforcement learning approaches. These methods included off-policy deep Q-network (DQN) and on-policy proximal policy optimization (PPO), with the latter being proved highly effective in enhancing the timeliness of the transmitted information.

Regarding the beam-splitting functionality of programmable metasurfaces, numerous studies have investigated the performance of multi-user communication systems employing a non-orthogonal multiple access (NOMA) scheme based on a beam-splitting UAV-mounted RIS [15], [16], [17]. Additionally, the authors in [18] proposed an algorithm that optimizes the UAV deployment, RIS configuration, and BS's transmit power to enhance the energy efficiency of a multi-user system supported by a beam-splitting UAV-mounted RIS. Furthermore, considering a recently emerged multiple access scheme called rate-splitting multiple access (RSMA), the authors in [19] investigated the outage probability, the block error rate (BLER), and the achievable weighted sum rate of RSMA in UAV-mounted RIS networks by jointly optimizing the RSMA parameters, the 3D coordinates of the UAV-mounted RIS, and the induced phase shifts from the RIS's reflecting elements.

While the existing literature primarily focuses on beam-steering and beam-splitting functionalities, the research on absorbing metasurfaces remains relatively limited, particularly in the context of UAV-assisted networks. In more detail, absorbing metasurfaces can be effectively employed for a multitude of purposes within the communication environment, such as reducing signal strength in directions and regions where the presence of a malicious user is suspected, energy harvesting, Doppler effect mitigation, and interference reduction [20], [21], [22], [23]. Therefore, investigating such metasurfaces is crucial to address this gap in the current literature and align with the objective of exploring practical implementations of a fully-functional programmable wireless environment (PWE) based on UAVs [6], [24]. Furthermore, in UAV-assisted networks, the fluctuating motion of UAVs introduces uncontrolled variations that can significantly impact communication efficiency, as the metasurface response is greatly influenced by the angle of arrival of incident waves [25]. However, to the best of the authors' knowledge, no work has been conducted to experimentally validate the effect of UAV fluctuations on a communication system that relies on a UAV-mounted metasurface. Thus, to comprehensively understand and validate the mobility effects of UAV fluctuations on a communication system relying on UAV-mounted metasurfaces, experimental validation becomes imperative since it will provide valuable

insights into the practical implementation of UAV-mounted metasurfaces in real-world scenarios.

### B. CONTRIBUTION

In this work, we perform a comprehensive evaluation of communication channels facilitated by UAV-mounted metasurfaces, considering real-world scenarios and addressing the impact of UAV mobility on the system performance. In more detail, our contribution is the following:

- We conduct a rigorous theoretical analysis that incorporates the impact of UAV mobility, including positioning, alignment, and orientation, on the performance of the communication channel within the transmitter-metasurface-receiver configuration.
- In contrast to the existing literature that predominantly focuses on beam-steering metasurfaces, our study and the applicability of our modeling extends to absorbing metasurfaces, filling a gap in the current research landscape.
- To validate the theoretical findings and demonstrate the real-world performance of UAV-mounted metasurface-enabled communication channels, we provide results from a controlled experimental investigation conducted in an anechoic chamber.

To this end, through thorough theoretical modeling and experimental procedures, our work contributes to the advancement of metasurface technology and paves the way for the development of more efficient and versatile UAV-enabled communication systems.

The structure of this paper is as follows: Section II discusses the network architecture and its components, providing an in-depth analysis. Section III delves into the application of the Fresnel-Kirchhoff diffraction theory as a physical optics model for metasurface wavefront diffraction and wireless links; the model is fed with the metasurface parameters acquired by unit-cell level full-wave EM simulations. Moreover, In Section IV, the experimental setup, parameter sensitivity analysis, and path loss measurements are presented for monostatic scattering off a fluctuating UAV-mounted absorbing metasurface. Finally, Section V provides concluding remarks on our work.

## II. SYSTEM ARCHITECTURE

The examined network architecture encompasses a comprehensive framework comprising a *UAV orchestrator* and *UAV-mounted static metasurfaces*, which collectively contribute to the establishment of robust wireless communication links, as illustrated in Fig. 1. In more detail, Fig. 1 provides a visual representation of the key components within the network architecture, showcasing the seamless integration of the UAV orchestrator and the static metasurfaces. Through the orchestrated efforts of these components, the network architecture aims to enable efficient and reliable wireless communication, overcoming obstacles and enhancing connectivity in various scenarios and environments. It should be mentioned that the presented architecture not only

prioritizes the reliability and efficiency of communication but also emphasizes safety, high performance, and optimal energy utilization.

### A. UAV ORCHESTRATOR

The UAV orchestrator is a pivotal software component, consisting of three main elements: the UAV Traffic Manager (UTM), responsible for UAV placement and considering various restrictions and feedback; the UAV Energy Manager (UEM), ensuring effective power management and recharging of UAVs; and the Network Monitor, which is well-informed about the quality-of-service (QoS) requirements of each user and enables the identification of malicious transmitters in the service area.

- UAV Traffic Manager (UTM): The UTM is the main brain of the orchestrator. It is responsible for the placement of the UAVs while taking into account various restrictions and feedback from other components, such as the UAV energy requirements, the client QoS requirements, the weather conditions, and the airspace authorization. Moreover, it is responsible for grouping the UAV network to allow the division of the network for different use cases.
- UAV Energy Manager (UEM): One of the major limitations in the UAV operation is their energy needs. The UEM is responsible for preventing power outages of UAVs and handling their recharging through charging stations [26] or returning safely to the base. The decisions made by the UEM are delivered at the UTM for appropriate mobility actions and resource allocation.
- Network Monitor: The network monitor is aware of the QoS needs of each specific client, as well as the needs of the different use cases that would enable possible UAV network synergetic procedures. Therefore, it informs the UTM to take appropriate actions on the UAV placement and UAV grouping, as well as about the existence of malicious transmitters in the service area and their characteristics.

### B. UAV-MOUNTED METASURFACES

In the proposed network topology, to provide the required services, a UAV swarm is licensed to operate under the command of the UAV orchestrator. Each UAV in the swarm can dynamically carry a static metasurface, allowing for specific wave manipulation functionalities [24]. Specifically, when the demanded network services are determined, the UAV orchestrator initiates the deployment of the metasurfaces at the users' premises, providing the necessary assistance and communication augmentation. Following the orchestration planning phase, a subset of UAVs in the swarm retrieves the designated metasurface units and then moves to specific positions dictated by the orchestrator, e.g., blocking the channel between an identified malicious transmitter (Tx) and a network-user receiver (Rx), while respecting any positioning limitations by the Network Monitor and the UAV Traffic Manager. Once in position, the channels are automatically
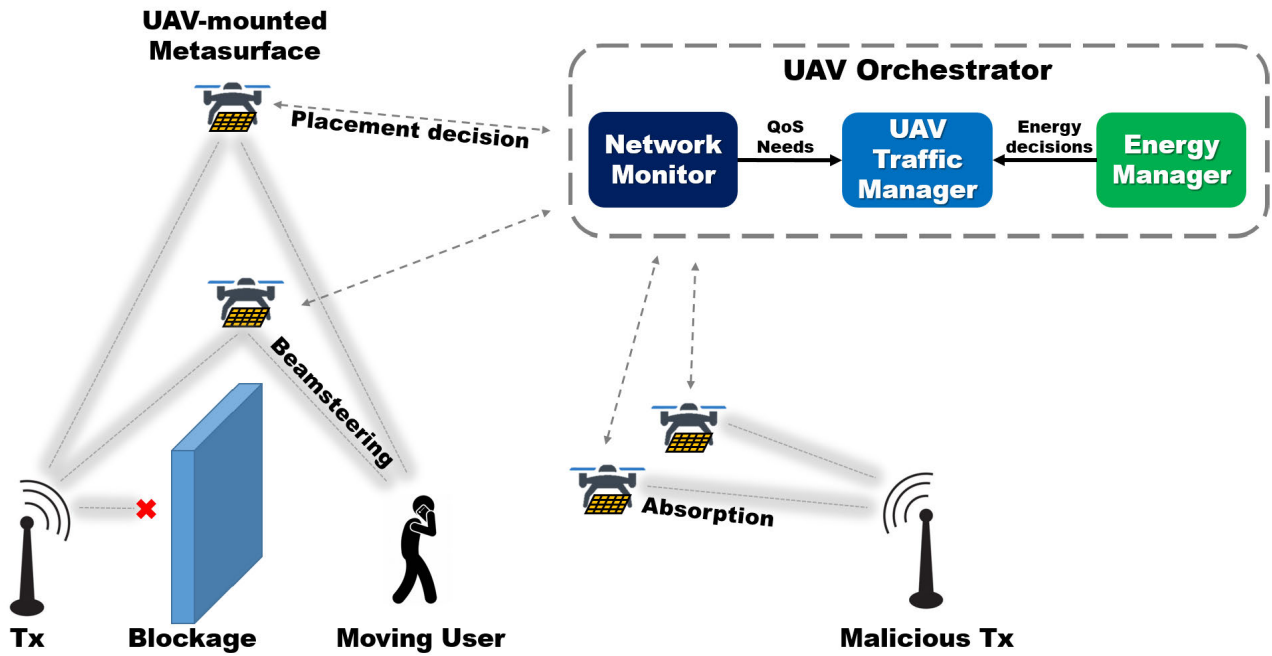
**FIGURE 1.** UAV-mounted metasurfaces operation.

deployed without the need for further deliberation. Finally, it should be highlighted that each metasurface is carefully mounted in each UAV, in order to not obstruct the UAV's propellers or significantly affect its aerodynamic properties and hence its stability and energy efficiency; depending on the application and its aperture relative to the drone size, the metasurface could be placed vertically or horizontally.

*Absorbing Metasurface:* Within the network architecture described above, our work focuses on enhancing communication security, particularly in the context of countering a malicious transmitter (malicious Tx) attempting to transmit harmful messages to a network user (receiver Rx). To effectively address this challenge, we strategically deploy UAV-mounted metasurfaces that perform the absorption functionality. These metasurfaces act as a protective barrier between the user and the malicious Tx, preventing malicious communication and ensuring uninterrupted and secure communication between legitimate nodes [20], [27]. Compared to scattering or deflecting plates, absorbing metasurfaces have the advantage of spectral selectivity or large absorption bandwidth (in frequency and direction of incidence), depending on their design and the application scenario. Another envisaged application of UAV-mounted absorbing RIS is harvesting of directed or backscattered EM waves, which can used to power the UAV and/or RIS operation, thus increasing battery/flight time.

In our approach, we utilize multifunctional metasurfaces, manufactured with printed-circuit-board (PCB) technology comprising three metallization layers and using lumped resistor and capacitor (*RC*) elements to tune the absorption

resonance frequency and depth [28]. The PCB dielectric substrate is the high-frequency graded Panasonic Megtron7N material, characterized by a relative permittivity ($\epsilon_r$) of 3.35 and a loss tangent ($\tan \delta$) of 0.002; the dielectric thickness between the patches and backplane layer, being critical for the resonance, is 2.14 mm.

- The **top metallization layer** of the metasurface structure consists of a symmetrical arrangement of a $2 \times 2$ array of square copper patches. Each patch has dimensions of 3.95 mm $\times$ 3.95 mm, forming a square periodicity with a lattice constant of 9 mm. This periodicity corresponds approximately to $\lambda_0/7$ at the frequency of 5 GHz, enabling effective control over the incident EM waves.

- The **middle metallization layer** serves as the metasurface backplane, allowing the structure to reflect the incoming waves while minimizing transmission. This layer plays a crucial role in blocking the signals from the malicious Tx and preventing their propagation towards the user.

- In the **bottom metallization layer**, surface-mounted devices (SMD) or application-specific integrated circuits (ASIC), i.e., 'chips', can be integrated into the metasurface board [2]. This innovative design allows the loads to be concealed beneath the backplane without interfering with the incident EM waves or obstructing the aperture. The connection between the front-side patches and back-side loads is established using through vias, ensuring efficient electrical connections. In our static metasurface implementation, fixed-value SMD resistors and capacitors were used.
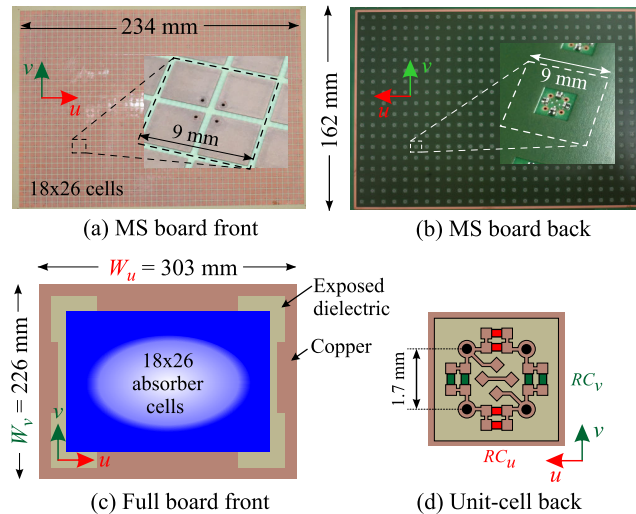
**FIGURE 2.** Photographs of the absorbing area of the metasurface with unit cell close-up insets, (a) front and (b) back side. (c) Schematic of the full aperture of the metasurface treated as a non-uniformly configured flat 'scatterer'; the blue area corresponds to the absorbing aperture. (d) Arrangement of the SMD loads along the board's two principal axes, *u* (long side) and *v* (short side).

The family of fabricated metasurface boards consists of a rectangular array of 18 × 26 uniformly configured square absorbing unit cells, resulting in an effective aperture size of 162 mm × 234 mm, as illustrated in Figs. 2(a) and 2(b). The local coordinate system of the metasurface board is *uvw*, where $\hat{u}$ and $\hat{v}$ are the unit vectors along the long and short side of the board, respectively, and $\hat{w}$ is the outward-pointing normal unit vector. Differently valued *RC* SMD pairs are assembled on the *u*- and *v*-slots in the bottom metallization layer, as shown in Fig. 2(d), to achieve two distinct absorber resonances near 5 GHz. In the absorbing board used in this work, we selected $RC_u = 100 \ \Omega \parallel 0.8$ pF and $RC_v = 22 \ \Omega \parallel 2.7$ pF, which produce absorption resonances near 5.3 and 4.7 GHz, respectively. It should be highlighted that this architecture strictly prohibits back-side transmission, minimizes diffraction orders (cell width is considerably subwavelenth, $\lambda/7$), and ensures independent polarization control (with negligible cross-polarization coupling) with loads placed along the *u* and *v* principal axes of the board.

Fig.2(c) illustrates that the full PCB board is bordered by 3.2 cm-wide regions on each of the four sides of the absorbing aperture consisting of 18 × 26 cells. This was a result of the fabrication technology employed and the mounting considerations in the automated positioner utilized in [28]. In the experimental setup of the current study, it was chosen not to coat these regions with absorbing material to avoid compromising the airflow and stability of the UAV. However, it should be noted that these borders are reflective, consequently reducing the absorption capabilities of the overall effective aperture in comparison to considering only the absorbing aperture. Additionally, while simpler models could have sufficed for a homogeneous metasurface aperture, the

non-uniformity introduced by these regions necessitates the use of a more advanced model. Specifically, the full aperture can be treated as a non-uniformly configured flat 'scatterer', consisting of three types of materials:

- **Absorbing metamaterial unit cells**, blue color in Fig. 2(c). For these highly dispersive regions, when the frequency, polarization, and incidence direction are on-resonance, full absorption occurs; otherwise, the cell reflects with a complex nonzero coefficient.
- **Copper-clad regions**, brown color in Fig. 2(c). These behave like a dispersion-less 'short-circuit', i.e., introduce a −1 reflection coefficient (full reflection and 180° phase retardation) for all frequencies, directions, and polarizations.
- **Exposed metal-backed dielectric regions**, beige color in Fig. 2(c). These areas give high reflection magnitude with a mild phase dispersion that depends on the frequency, polarization, incidence direction, and dielectric (thickness and permittivity).

To evaluate the performance of the absorbing metasurface in the examined communication scenario, we consider the appropriate complex-valued scattering-matrix element, i.e., $S_{21}$ (where ports 1 and 2 correspond to Tx and Rx antennas), where a minimum in $|S_{21}|$ corresponds to maximum absorption for the metal-backed reflective metasurface. As shown in [28], the same metasurface can be used for other functionalities, realized by different arrangements of the SMD loads placed in each cell on its back-side. For instance, two-beam splitting of a plane wave can be achieved with a meta-grating 1-bit encoded patterning, i.e., selecting two values of capacitors that introduce a reflection-phase difference equal to $\pi$ at the operating frequency. As another example, anomalous reflection, also known as beam steering, can be achieved with 2-bit digital coding (four phase-states) in the unit cell reflection [29]. In all cases, the overall metasurface response is dictated by the 'local' reflection amplitude and phase in its unit cells. It is stressed again that the latter is highly dispersive, thus rendering the overall metasurface board efficiency for a given functionality a function of local metamaterial configuration (e.g., value of RC loads in each cell), but also of frequency, direction, and polarization of the impinging wave.

## III. THEORETICAL ANALYSIS

In this section, an overview of the Fresnel-Kirchhoff diffraction theory is presented, which serves as a physical optics (PO) model utilized for the analysis of wavefront diffraction in the context of an arbitrarily configured metasurface. The focus is placed on formulating the diffraction theory to accurately calculate the path loss in wireless links between Tx and Rx antennas directed towards the metasurface aperture. Additionally, the application of PO models in wireless propagation channels featuring metasurfaces is discussed, with emphasis on capturing the effect of mobility (positioning and orientation) of Tx, Rx, and/or the metasurface. Finally, the calculation of parameters for the path loss model is performed

by employing a full-wave EM simulation of the absorbing metasurface unit cells.

## A. PHYSICAL OPTICS: DIFFRACTION BY IMPERFECTLY ABSORBING APERTURE

In the realm of microwave applications, metasurfaces can be considered as flat scatterers with small aperture diameters. However, in wireless communication links facilitated by metasurfaces, there may exist cases where the distances can be comparable to or even smaller than the aperture diameter, necessitating a reevaluation of conventional far-field approximations for accurate path loss calculations [30]. Particularly, when considering the network's UAV orchestrator, it is crucial to acknowledge that the UAV-mounted metasurface may not always be situated in the EM far-field of both the transmitter and the receiver; the radiating near-field distance [31] is greater than a couple of wavelengths which, in these microwave bands, is longer than the UAV size that should in all cases be respected by the Orchestrator. Consequently, the development of path loss models applicable to both far-field and near field conditions becomes essential, as they will enable a comprehensive understanding of the metasurface's behavior in diverse scenarios and facilitate optimal placement decisions by the UAV orchestrator.

In the context of metasurface-assisted communications, PO, also known as wave optics, offers a formal theory that strikes a balance between computational complexity and accuracy. PO serves as an intermediate solution, bridging the gap between rigorous vector full-wave EM modeling and simplified far-field theorems such as the Friis and radar equations [31]. A key aspect of PO is the derivation of a complex-valued "transparency function" defined on the metasurface aperture. This function establishes a connection between the phase and amplitude of incident and scattered fields, and is related to the local plane-wave reflection coefficient. Homogenization techniques can further enhance the efficiency of phase-profiled metasurfaces [32]. To this end, by leveraging PO, our study focuses on modeling the diffraction phenomena in arbitrarily profiled metasurfaces, i.e., metasurfaces that may encompass regions with absorptive and/or reflective properties. This comprehensive approach allows for a thorough representation of the metasurface's behavior, providing valuable insights into the interaction between incident waves and the metasurface, and shedding light on its functionality and performance [32].

Within the framework of PO, various well-established tools are employed, as outlined in [33]. These tools include the Huygens-Fresnel principle (HFP), which treats each point on a wavefront as a secondary source of forward-propagated spherical wavelets; the Helmholtz-Kirchhoff integral theorem (HKIT), derived from Green's theory, used for evaluating the field given its value and gradient on an arbitrary surface; the Fresnel-Kirchhoff diffraction (FKD) formula, which is a specialization of HKIT in the absence of sources and for point-source illumination; and the Rayleigh-Sommerfeld

diffraction (RSD) formula, which addresses inconsistencies of the FKD but is limited to flat apertures.

While these tools have been extensively employed in the study of diffraction effects in optical lenses and metal-backed microwave metasurfaces like reflectarrays or gratings [34], [35], their simplicity and elegance make them suitable for many wireless communication scenarios within the microwave to mmWave bands. Furthermore, considerations of vector fields can be accommodated through dyadic or vector formulations of Green's theorem, striking a balance between complexity and accuracy [30], [36]. Despite the specific conditions associated with each PO theorem, they often converge to similar solutions, especially for planar surfaces, refracting or reflecting elements, and far-field antennas located close to the broadside of the aperture, where the rays cast from the antenna arrive at oblique angles $\theta < 45°$, with $\theta = 0$ and $\theta = 90°$ denoting the normal and grazing directions, respectively.

In this study, we assume a planar UAV-mounted metasurface illuminated by a spherical wavefront, and we employ the scalar Fresnel-Kirchhoff diffraction (FKD) formula to calculate the scattered field amplitude. To simplify the method employed, we will present it in a 2D case, i.e., in a meridional cut-plane of the metasurface, which is easily extendable to 3D. Specifically, the Tx-metasurface-Rx arrangement is illustrated in Fig. 3 where, based on the scalar form of Babinet's principle [31], [33], [37], the scattering from the reflecting metasurface is equivalent to that from a refractive aperture in an opaque screen. This setup can be toggled between reflection and transmission modes by mirroring the image space at the flat metasurface plane. To compute the wireless channel path loss, we consider two points on either side of the metasurface as the Tx and Rx antennas, decoupled and co-polarized with directive radiation patterns, their maximum gain orientation defined by unit vectors $\hat{\alpha}_{\text{Tx/Rx}}$, Fig. 3(b). The arbitrary metasurface configuration is visualized by the colored squares in the bottom-right hand inset in Fig. 3(b), where different colors denote magnitude and/or phase of the transparency function in each cell. By analyzing this configuration, we can assess the path loss in the wireless channel and gain valuable insights into the performance of metasurface-assisted communication systems.

With reference to the parameters defined in Fig. 3(b), the FKD formula for the calculation of the complex E-field at the receiver position, $E_{\text{Rx}}$, is an integration of the scattering (diffraction) from all infinitesimally small regions of the aperture. This integration can be illustrated by scanning the auxiliary point Q across the metasurface in the $xy$-plane, i.e.,

$$E_{\text{Rx}} = \frac{F_{\text{Tx}}}{j\lambda} \iint_{\text{Q@MS}} (\sqrt{G_{\text{Tx}}}e^{j\phi_{\text{Tx}}})(\sqrt{G_{\text{Rx}}}e^{j\phi_{\text{Rx}}})$$

$$\Gamma_{\text{MS}} \times \Psi \times \frac{\exp[jk(r_1 + r_2)]}{r_1 r_2} \, \mathrm{d}x\mathrm{d}y, \tag{1}$$

where the calculated intensity $|E_{\text{Rx}}|^2 = P_{\text{Rx}}(4\pi/\lambda^2)$ is related to the effective power received at Rx, $r_{1/2} = |\vec{r}_{1/2}|$ is the distance Tx-Q/Q-Rx, $k = 2\pi/\lambda$ is the medium
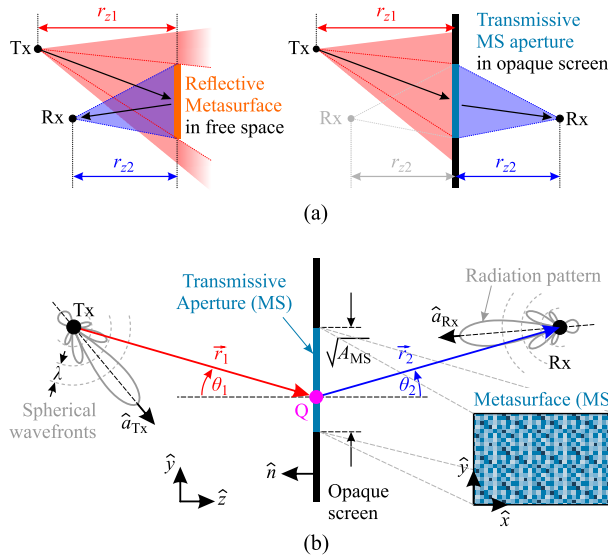
**FIGURE 3.** (a) Equivalence of scattered scalar fields in the 'image space' between reflective and transmissive cases; blue cone represents the illuminated aperture contributing to diffraction at point Rx. (b) Schematic configuration for Fresnel-Kirchhoff diffraction (FKD) in 2D. Arbitrarily-oriented same-polarization Tx and Rx antennas in far-field with known emitted field at Tx and computed received field at Rx by sweeping auxiliary point Q across the aperture; a flat transmissive metasurface occupies the aperture in the $xy$ plane, which modifies the amplitude and phase of the wavefront.

wavenumber, the constant $|F_{Tx}|^2 = P_{Tx}/4\pi$ is the effective isotropic radiated power (EIRP) of Tx, $G$ and $\phi$ are the gains and phases of the Tx/Rx antenna patterns, $\Gamma_{MS}$ is the complex-valued transmission (mirrored reflection) coefficient, and $\Psi \in [0, 1]$ is the "obliquity factor" defined by the angles between the unit vectors

$$\Psi = -\frac{1}{2}\hat{n} \cdot (\hat{r}_1 + \hat{r}_2) = \frac{1}{2}(\cos\theta_1 + \cos\theta_2), \quad (2)$$

where $\hat{n}$ is the outward-pointing unit vector of the metasurface and $\hat{r}_m = \vec{r}_m/r_m$, $m = \{1, 2\}$; the maximum value of $\Psi \to 1$ is attained for $\theta_{1/2} \to 0$, i.e., at normal incidence.

We stress that the values of all parameters in Eq. (1) (with the exception[1] of $F_{Tx}$) depend on the position of the auxiliary point Q($x, y$) on the metasurface aperture and on the direction vectors $\vec{r}_{1/2}$, i.e., on the incident and scattered "ray" angles, $\theta_{1/2}$, defined by the triplet Tx, Rx, and Q, which represent points defined in 3D space. Therein lies the usefulness of this PO model to study the mobility effect, i.e., positioning and pointing accuracy, in wireless channels enabled by UAV-mounted metasurface, especially in the near-field zone.

Special note must be given to the complex-valued $\Gamma_{MS} = \Gamma_{MS}(x, y; \lambda, \theta_1)$, in order to highlight the metamaterial's (i) spatial configuration and locality, i.e., the unit cell configuration at the given Q($x, y$) point, and (ii) frequency and angular dispersion. In this work, $\Gamma_{MS}$ is the "transparency function" of the aperture, defined at the beginning of this

---

[1]The FKD formula is derived for illumination from a point-source of power proportional to $|F_{Tx}|^2$, producing a spherical wavefront.

section; for passive metasurfaces $|\Gamma_{MS}| \le 1$ and for efficient absorption, $|\Gamma_{MS}| \to 0$. Finally, do note that $\Gamma_{MS}$ is also a function of polarization, which is omitted in the presently studied scalar case, assuming that Tx/Rx antennas are co-polarized and with a relative orientation to the metasurface so that cross-polarized scattering is negligible.

### B. PATH LOSS MODEL BASED ON SCALAR FRESNEL-KIRCHHOFF DIFFRACTION

Using optics terminology, the setup depicted in Fig. 3 is a point-object/point-image formation. Using wireless propagation terminology, Eq. (1) enables the calculation of the path loss between far-field Tx (object) and Rx (image) antennas, after scattering from a metasurface in free-space, which is equivalent to a lens in an opaque aperture, i.e.,

$$L_{FKD} = \frac{P_{Rx}}{P_{Tx}} = \left(\frac{\lambda}{4\pi}\right)^2 \times \left|\frac{E_{Rx}}{F_{Tx}}\right|^2. \quad (3)$$

The received field $E_{Rx}$ is measured in V/m or $\sqrt{W}$/m, while the transmitted field $F_{Tx}$ is measured in V or $\sqrt{W}$. The calculation is outlined in Algorithm 1.

It can be shown that the path loss using the FKD formula, described in Eq. (3), reduces to the standard radar equation [31] when the metasurface aperture diameter is small compared to the distances $r_{1,2} \gg \sqrt{A_{MS}} \gg \lambda$. In this case, all parameters in the integrand of Eq. (1) can be assumed as lumped constants so that, using Eq. (3) for the path loss, we derive

$$L_{Radar} = \frac{P_{Rx}}{P_{Tx}} = G_{Tx}G_{Rx}\frac{\sigma}{4\pi}\left(\frac{\lambda}{4\pi r_1 r_2}\right)^2, \quad (4)$$

where $\sigma$ is the bistatic radar cross section (RCS) of the scatterer, e.g., $\sigma = 4\pi(A_{MS}/\lambda)^2 \times |\tilde{\Gamma}_{MS}\tilde{\Psi}|^2$. The tilde in these expressions denotes an effective value, i.e., a spatial weighting across the metasurface. Employing the stationary-phase approximation is crucial in this spatial weighting, which involves finite integral of a complex function with a rapidly oscillating phase term, e.g., the Type-1 and 2 integrals in Section III-B in [30]; for quasi-uniformly configured apertures, $||\nabla\Gamma_{MS}|| \ll 1$, the integral is equal to a simple average of $\Gamma_{MS}$ of the cells. For instance, in the case of a flat rectangular PEC plate at normal incidence, we get $|\tilde{\Gamma}_{MS}| = |\tilde{\Psi}| = 1$ and $A_{MS} = W \times H$. Note that the same qualitative result as in Eq. (4), bearing the product of squared distance in the denominator, has been found in related works [5], [9], [13], [38], which verifies the generality of this methodology even further.

Finally, the Friis transmission equation can be extracted from the radar equation invoking the method of images [31]: By folding the optical axis in the half-distance between the Tx/Rx antennas, so that they are co-located, we assume a PEC sphere enclosing them at its center. This sphere is equivalent to the scatterer of the radar equation so that its RCS is equal to its (inner) surface, i.e., $\sigma = 4\pi\rho^2$, where $\rho = d/2 = r_1 = r_2$ is the half-distance between the Tx-Rx antennas in

---

**Algorithm 1** Path Loss via FKD Formula

**3D space:** Define Cartesian coordinate system $xyz$;
**Metasurface geometry:** Discretize metasurface aperture in $N_Q$ domains identified by index $q$ and having infinitesimal area $ds_q$;
**Parameters:** Set wavelength $\lambda$;
**Metasurface EM configuration:** Define metasurface configuration on each $q$-domain via complex reflection coefficient $\Gamma_{MS,q}$ depending on $\lambda$ and incidence direction;
**Tx/Rx antennas:** Define positions and 3D radiation patterns (depends on $\lambda$); define Tx amplitude $F_{Tx}$;
**Initialize:** Total received field $E_{Rx} = 0$, $q = 1$;
**while** $q \leq N_Q$ **do**
> **Assign** point Q as the centroid of $q$-domain;
> **Compute** vectors $\vec{r}_{1/2}$ from points {Q,Tx,Rx} in 3D space;
> **Compute** obliquity factor $\Psi$ using Eq. (2) from unit vectors $\hat{r}_{1/2}$ and $\hat{n}$;
> **Compute** incidence angle $\theta_1$ from $\hat{r}_1$ and $\hat{n}$;
> **Compute** $\Gamma_{MS}$ from Q, $\lambda$ and $\theta_1$;
> **Compute** the gain and phase, $G_{Tx/Rx}$ and $\phi_{Tx/Rx}$ from $\hat{r}_{1/2}$ and Tx/Rx antenna patterns;
> **Assign** $B$ as the integrand of Eq. (1);
> **Compute** E-field at Rx from scatterer at Q illuminated by source at Tx:
> $E_q = F_{Tx}/(j\lambda) \times B \times ds_q$;
> **Add** to total field $E_{Rx} = E_{Rx} + E_q$;
> **Increase** $q = q + 1$;

**end**
**Result:** Total $E_{Rx}$ (complex scalar);
**Compute** path loss from Eq. (3).

---

free-space. Inserting these in Eq. (4) we get

$$L_{Friis} = \frac{P_{Rx}}{P_{Tx}} = G_{Tx} G_{Rx} \left( \frac{\lambda}{4\pi d} \right)^2. \qquad (5)$$

In Eq. (4) the antenna gains are assumed along the direction of the "cardinal ray" connecting Tx/Rx to the effective centroid of the scatterer, e.g., the black arrow(s) connecting Tx/Rx points in Fig. 3(a); for Eq. (5) the gains are along the direct ray connecting Tx/Rx.

### C. EXTENSIONS OF PHYSICAL OPTICS MODELING

Excluding the overarching scalar approximation in Eq. (1), the practical limitation is that $kr_{1/2} \gg 1$. Despite its simplicity, the FKD formula provides excellent agreement with measurements up to a moderate obliquity, $\Psi > 0.5$; this agreement is fair up to the radiative near field zone, $r_{1/2} \approx \lambda$, with inclusion of $1 + (1/jkr)$ factors in the integrand, that were simplified under the $kr_{1/2} \gg 1$ condition [33]. It should be pointed out this formula makes no assumptions on the shape of the aperture meaning that it can handle non-planar surfaces, e.g., arced or conformally curved metasurfaces;

the only limitation is that only regions of the metasurface (e.g., regions $q$ in Algorithm 1) that are in line-of-sight of both Tx and Rx are considered. The RSD formula is a more rigorously derived version of the HKIT, but is applicable only for flat surfaces, whereas the FKD applies to any shape and offers comparable results.

Next, we will outline how the basic concept of the FKD theory can be extended to different scenarios, relevant to wireless communications, RF imaging, and holography.

#### 1) FROM 2D SCALAR TO 3D VECTOR FORMULATION

It should be highlighted that computations with Eq. (1) can be performed in 3D using the same variables, under the scalar approximation. The various 2D angles and dimensions defined in Fig. 3(b), e.g., $\theta_{1/2}$, served only for clarity.

Furthermore, extending the scalar FKD formula to its vector counterpart means that the polarization of the antennas and the anisotropy in the metasurface response, i.e., in $\Gamma_{MS}$, must be properly accounted for. To this end, the vector version of Green's theorem or dyadic Green's functions can be employed for the derivation, leading to the well-known Stratton-Chu and Franz formulas [36]. Even though the mathematical expressions and the underpinning 3D vector algebra can be daunting, it is worth pointing out that the resulting vector expressions bear remarkable resemblance to the scalar FKD formula of Eq. (1). For instance, the corresponding Eq. (21) in [30], except from the antenna-coupling (first term), includes a surface-integration across the metasurface aperture with a complex valued integrand wherein we identify the same parameters: the distances $d_{Tx/Rx} \equiv r_{1/2}$ in the phase-term and as a product in the amplitude denominator, the complex reflection coefficient $\Gamma_{ref} \equiv \Gamma_{MS}$, the gains, and even the same expression for the obliquity factor, i.e, the last term in Eq. (23) in [30]. The core difference is the inclusion of polarization of the Tx/Rx antennas via the factor $\Omega_{ref}$, which tends to unity for co-polarized antennas, low cross-polarization reflection from the metasurface, and low obliquity ('electrically small' regime).

#### 2) FROM CONTINUOUS TO DISCRETIZED APERTURES

In the case of a metasurface aperture discretized in a set of finite-sized regions, e.g., in a grid of subwavelength-sized unit cells, as in the right-hand inset in Fig. 3(b), the surface integral of Eq. (1) reduces to a summation over the individual unit cells, i.e.,

$$\iint_{Q@MS} U(x, y)\, dx dy \approx \sum_{q=1}^{N_q} U(x_q, y_q) ds_q, \qquad (6)$$

where $U$ is the complex integrand and $q$ is the index of the cell whose aperture is centered at $(x_q, y_q)$ and whose area is $ds_q \ll \lambda^2$; the cells are usually square and arranged in a square grid in the $xy$-plane. Note that here lies an approximation introduced via PO, stating that the continuous function $U(x, y)$ in the integrand, that is 'sampled' to $U(x_q, y_q)$, is an effective surface-averaged quantity related to the local unit

cell properties, i.e., to the value of $\Gamma_{MS}(x_q, y_q)$, through a homogenization procedure [4].

### 3) MOVING RX AND/OR TX ANTENNAS TO THE FAR-FIELD

In the present form of the FKD formula, Eq. (1), it is assumed that both Tx and Rx antennas are at finite distances $r_{1/2}$ which is equivalent to assuming spherical wavefronts emitted from Tx and received by Rx. Moreover, in most passive metasurface configurations, reciprocity can be invoked to swap Tx/Rx antennas, without change to the response.

Now, the FKD formula can also be used to compute the far-field scattering pattern $E(\theta, \varphi)$ [29] and extract information like lobe and null directions, beamwidth, side-lobe level, etc. Therefore, Eq. (1) is used assuming that the Rx antenna is moved to the far-field, i.e., $r_2 \rightarrow \infty$ (so that only its direction matters), and normalizing the integrand by $\sqrt{G_{Rx}}e^{j\phi_{Rx}}/r_2$.

In a similar modification, moving the Tx antenna to the far-field, $r_1 \rightarrow \infty$, is equivalent to having a plane-wave illuminating the metasurface from a given direction angle pair $(\theta, \varphi)$.

### 4) SPOT DIAGRAMS AND HOLOGRAPHY

The FKD formula can be directly used for the computation of the scattered electric near field, i.e., at distance $r_2 \geq \lambda$, with reasonable accuracy. For instance, by scanning the Rx point across a plane normal to the $z$-axis at $z = z_0$ one can evaluate the spot diagram $E_{Rx}(x, y, z_0)$. This is helpful for focusing metasurface configurations, e.g., when a plane wavefront is focused on the aperture of a horn antenna, or for holographic applications, e.g., when the 'wavefield' scattered from a meta-hologram (phase- and/or amplitude-encoded metasurface) coherently diffracts in 3D space reconstructing the 'object' stored in the hologram [39].

### 5) GENERALIZATION AND EQUIVALENCE TO HFP

From what we presented so far, the illumination is from a point source resulting in a spherical or plane wavefront, for finite or infinite $r_1$, respectively. In a further extension of the FKD formula, the illuminating source can be an arbitrary wavefront (non-spherical) provided that its complex value is properly defined on the metasurface aperture. In this case, the spherical wave $F_{Tx}e^{jk_0r_1}/r_1$ and the Tx antenna pattern in Eq. (1) are replaced by $E_{inc}(x, y)$ in its integrand. It can now be inferred that this is equivalent to the HFP (which can be derived by the first RSD formula for a flat aperture [33]) that computes the field anywhere in image space as an interference of spherical 'wavelets' scattered from all points in the aperture. Each one of these wavelets is equal to the local incident field weighted with the local effective complex-valued reflection coefficient, i.e., $E_{scat}(x, y) = \Gamma_{MS}(x, y)E_{inc}(x, y)$, thus it stands that

$$E_{Rx} = \frac{1}{j\lambda} \iint_{Q@MS} E_{scat} \frac{e^{jk_0r_2}}{r_2} \cos\theta_2 \, dxdy, \qquad (7)$$

where an isotropic receiver has been assumed, $\sqrt{G_{Rx}}e^{j\phi_{Rx}} = 1$, and the obliquity factor $\Psi$ depends only on the scattered angle $\theta_2$, according to the first RSD formula.

When using the HFP in the form of Eq. (7), i.e., for an arbitrarily-shaped incident wavefront, attention must be paid to the $E_{inc}(x, y)$ definition. When the impinging monochromatic wavefront has a sufficiently high degree of spatial coherence (large local curvature radii), e.g., in the case of plane waves or point sources at $r_1 \gg \lambda$, the wavefront can be simplified to a set of geometric rays impinging on the surface. In contrary, when the wavefront is spatially incoherent, any interference just before the metasurface is crucial in a way that challenges the validity of the underpinning approximations, i.e., scalar fields, subwavelength sampling to form the equivalent transparency function $\Gamma_{MS}(x, y)$, etc.

### D. FULL-WAVE SIMULATION OF ABSORBING METASURFACE UNIT CELL

In this work, given the approximations already introduced by the scalar nature of the FKD theory and the absorptive response of the metasurface, we will directly link the effective/surface-averaged local reflection coefficient in the centroid of each unit cell $\Gamma_{MS}(x_q, y_q)$ to its value in the infinite periodicity case, given by Floquet theory. Note that the (imperfectly) absorbing metasurface studied here is less demanding compared to an anomalous reflector in this regard, as the low magnitude of the reflection coefficient is of importance, and not its phase.

We simulate the absorbing unit cell, as shown in Fig. 2, using CST Microwave Studio with their nominal $RC$ values as in [28], for both polarizations, and for a range of oblique incidence directions in the two principal planes of the cell ($u$ and $v$) that are perpendicular to its surface. In a regular desktop computer, e.g., an Intel i5-10400 CPU with 16 GB RAM, the broadband sweep simulations for one combination of geometric parameters of the unit-cell and for one incidence direction $(\theta, \varphi)_{inc}$, conclude in a few minutes; note that the $RC$ loads are incorporated using S-parameter lumped ports as described in [2], so that parametrically sweeping them does not incur any extra delay. The results are depicted in Fig. 4, where we witness the opposite behavior of TE and TM polarizations with respect to oblique angle for this particular cell topology, with through-vias: for TE polarization we have a change in the Q-factor of the resonance but the frequency is unchanged, whereas the opposite holds for TM (frequency changes with oblique angle, but Q-factor is relatively unchanged). This observation holds for both absorption resonances, near 4.7 and 5.3 GHz. Another interesting feature is that the 4.7 GHz resonance leads to perfect absorption ($|S_{TE}| < -30$ dB) not at normal incidence, but at an angle $\theta_{inc} \approx 20\text{-}25°$.

Most importantly, from Fig. 2 we evaluate the absorption 'angular spectrum' around normal incidence and conclude that, for both polarizations, the reflection magnitude is $-15$ dB (or less) for up to $\theta_{inc} \leq 30°$. This means that our scalar/isotropic FKD model is valid up to that angle;
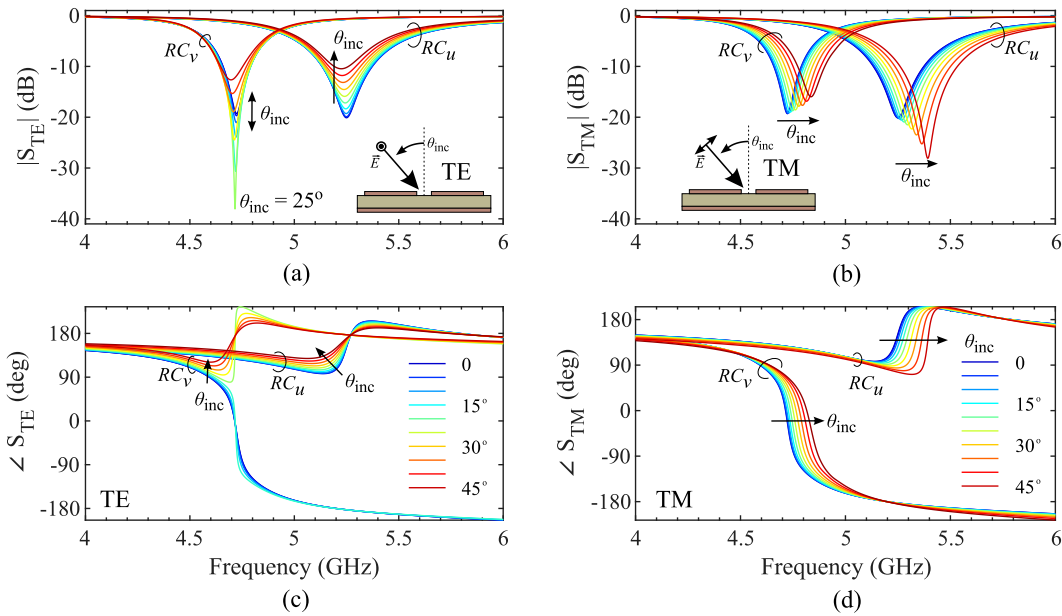
**FIGURE 4.** Full-wave simulated reflection spectra of the absorbing unit cell for various oblique incidence angles and both polarizations. The two lumped-load pairs, $RC_u$ and $RC_v$ in Fig. 2, produce absorption resonances near 5.3 and 4.7 GHz, respectively. Spectra of (a) TE magnitude, (b) TM magnitude, (c) TE phase, (d) TM phase.

accounting for the vector nature of the fields (and polarization) might improve the accuracy of the path loss prediction, but the difference will only be significant for Rx in the radiative near field zone, where $\theta_{inc}$ is large.

The reflection from the copper-clad regions is $\Gamma_{MS} = -1$ and the reflection from the exposed metal-backed dielectric regions can be computed by transmission line models [37]; it is an almost unitary reflection magnitude, $|\Gamma_{MS}| \rightarrow 1$ with a phase-shift that depends on frequency, incidence angle, polarization, and dielectric (thickness and permittivity).

## IV. EXPERIMENTAL SETUP, MODEL ANALYSIS, MEASURED RESULTS, DISCUSSION

In this section, we first describe the considered experimental setup, consisting of the monostatic scattering off a moving/UAV-mounted absorbing metasurface. Then, we perform a parameter sensitivity analysis of the setup using the FKD formula for the path loss between Tx/Rx antennas. Finally, we perform anechoic chamber path loss measurements and analyze/evaluate the results acquired.

### A. EXPERIMENTAL SETUP DESCRIPTION

One intended application of UAV-mounted absorbing metasurfaces is as a notch filter aimed to cancel out back-reflection from a malicious Tx, as shown in Fig. 1. An abstracted schematic of the experimental setup used to quantify this functionality is depicted in Fig. 5(a) and photographs of the manually flown UAV-mounted absorbing metasurface are depicted in Figs. 5(b) and 5(c). The setup in Fig. 5(a) is the 3D 'real-world' version of the 2D abstracted setup of

Fig. 3 that was meant to introduce the variables and the FKD formula; note that refraction is now swapped back to reflection, as shown in the left panel of Fig. 3(a).

In our experimental setup, the two antennas are positioned side by side with their aperture centers situated at points "Tx" and "Rx" in a plane perpendicular to the $z$-axis and facing the metasurface at directions $\hat{\alpha}_{Tx/Rx}$, respectively, in this case approximately parallel to $+\hat{z}$. The coordinate system's center, denoted as "O", is located at the midpoint between the antenna apertures. The metasurface is positioned at a distance $r_z$ along the $z$-axis from point "O", with its absorbing aperture facing the antennas in the $-\hat{z}$ direction. This configuration aims to maximize the path loss from the Tx to the Rx antenna by leveraging absorption within the metasurface. It is important to note that due to the dispersion characteristics of the absorbing metasurface, as depicted in Fig. 4, high path loss (i.e., high absorption) can only be achieved at specific frequencies and incidence angles. Contrastly, the metasurface behaves as a reflector when operating off-resonance. Lastly, in our experimental setup, we assume that the UAV's back-scattering is negligibly low compared to that of the metasurface aperture, even in a high absorption regime of 15 dB. This assumption is supported by measurements indicating an RCS signature $\sigma_{UAV} < 0.1$ m$^2$ at 5 GHz, significantly lower than the maximum RCS of 16 m$^2$ for a perfect electric conductor (PEC) plate of the same aperture size as our metasurface. The board weight is less than 1 kg.

### B. MOBILITY ANALYSIS

The path loss model based on the FKD formula, described in Eqs. (1) and (3), can be applied to the setup depicted in
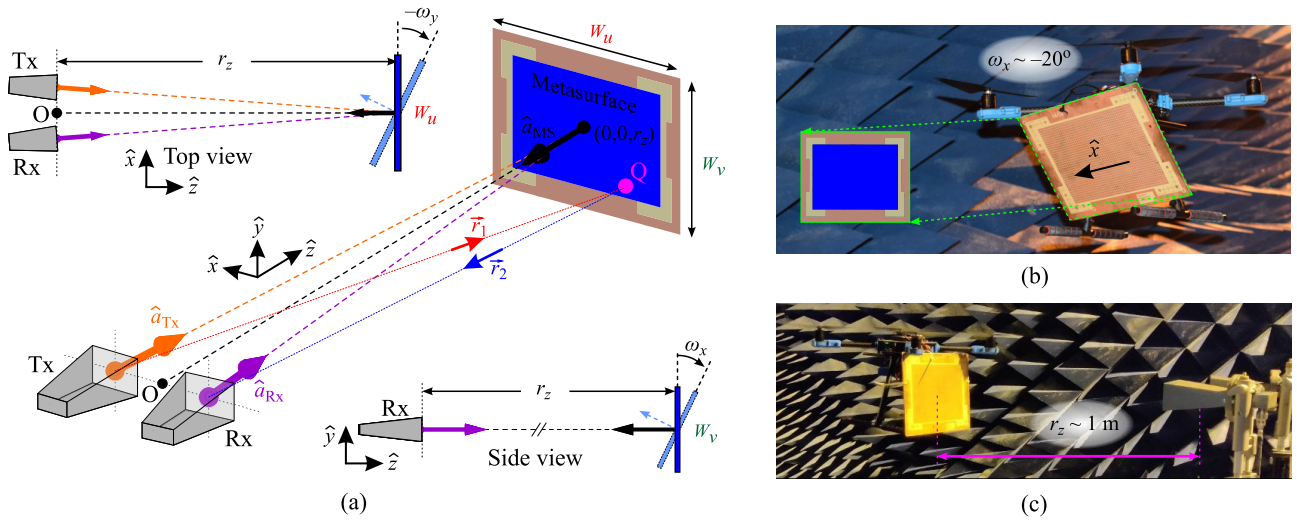
**FIGURE 5.** (a) Abstracted bird's eye view/schematic of the measurement setup for path loss from back-scattering on a flat metasurface: Two static horns are pointed to the reference position of the metasurface; the metasurface is attached to the UAV and its *xyz*-position and $\hat{\alpha}_{MS}$ orientation can change. The top-left and bottom-right insets depict the top-view and side-view of the setup, respectively, to clarify the metasurface orientation changes. (b),(c) Photographs of the UAV-mounted metasurface in flight in the anechoic chamber. In (b) the board is forward tilted, i.e., rotated by $-20°$ deg around $\hat{x}$ axis, and in (c) the distance from the antennas' plane is $r_z \sim 1$ m.

Fig. 5(a). In this 3D configuration, the magenta point labeled Q is scanned across the discrete set of unit cells, which in our implementation are the rectangles in Fig. 2(c). Under the superposition principle, we can compute how the overall board coherently scatters the spherical wavefront from the Tx antenna, by summing the scattered E-field by all the regions (absorbing cells or copper/exposed dielectric areas) on the location of the Rx antenna; this provides the path loss of the channel.

To assess the impact of UAV mobility on the channel path loss, we conduct a sensitivity analysis utilizing the FKD model, which grants control over the positioning and orientation parameters of the experimental setup. The findings of this analysis are depicted in Fig. 6. Further discussion on each individual parameter is provided below.

In Figs. 6(a) and 6(b), we evaluate the path loss as the distance $r_z$ between the upright metasurface and antennas plane is increased from the limit of the radiative near field zone, panel (a), up to the deep far-field zone, i.e., $r_z = 100$ m, panel (b); in all cases, both antennas were pointed to the centroid of the metasurface aperture. From the three curves we observe that rigorously discretizing the full aperture of the board and employing the FKD formula provides a different estimation from a simple averaging of its reflection (radar equation). Specifically, we see that even though the absorbing cells each contribute to approximately 20 dB absorption (Fig. 4) the final path loss compared to a same-aperture reference PEC plate is only 6.5 dB lower. As discussed in Section II-B, this is attributed to the borders of the metasurface board which are fully reflecting with a phase that depends on the material, i.e., if the region has copper cladding or exposed metal-backed dielectric. It should also be noted that the radar equation, which is described in Eq. (4) and

assumes a surface-averaged/weighted reflectivity from all the board, produces a 3.5 dB more optimistic path loss prediction. Its prediction can be corrected by applying a stationary-phase technique for the spatial weighting [30], which however is technically equivalent to using the FKD. Finally, we stress that it is crucial to accurately compute the *relative* phase of each individual scatterer, including the absorbing unit cells, copper, or exposed dielectric areas on the board, otherwise an up to 4 dB error in the path loss can be introduced, as exemplified by the discrepancy observed in the radar equation.

In Fig. 6(c), we study the effect of UAV movement in the plane transverse to the z-axis, i.e., as the UAV flies over/under or to the left/right of the point where the Tx/Rx antennas are targeted. We choose the same scenario as the one to be performed in the anechoic chamber, i.e., the UAV flying at a distance of only 1 m from the antennas plane; the metasurface is upright and results are normalized to the 33 dB path loss from the optimal alignment in Fig. 6(a). From the contour lines in Fig. 6(c), which are at 1 dB intervals, it can be observed that this absorbing metasurface has a 3 dB pointing-tolerance of $\Delta\theta \approx 15°$. Note that this chart is practically independent of distance $r_z$, meaning that similarly small transverse displacements due to UAV fluctuations, i.e., of a few tens of cm, will lead to negligible extra losses in longer distances compared to the ones considered here.

In Fig. 6(d), we investigate the effect of tilting of the metasurface around the x-axis (forward/backward) and/or around the y-axis (sideways), whereas rotation around the z-axis was not considered, since it can be modeled with co/cross-polarized reflection from the metasurface (angle between the local *uv* axes of the metasurface board with respect to the *xy* axes of the global coordinate system). Note that the metasurface titling is with respect to the global coordinate system and
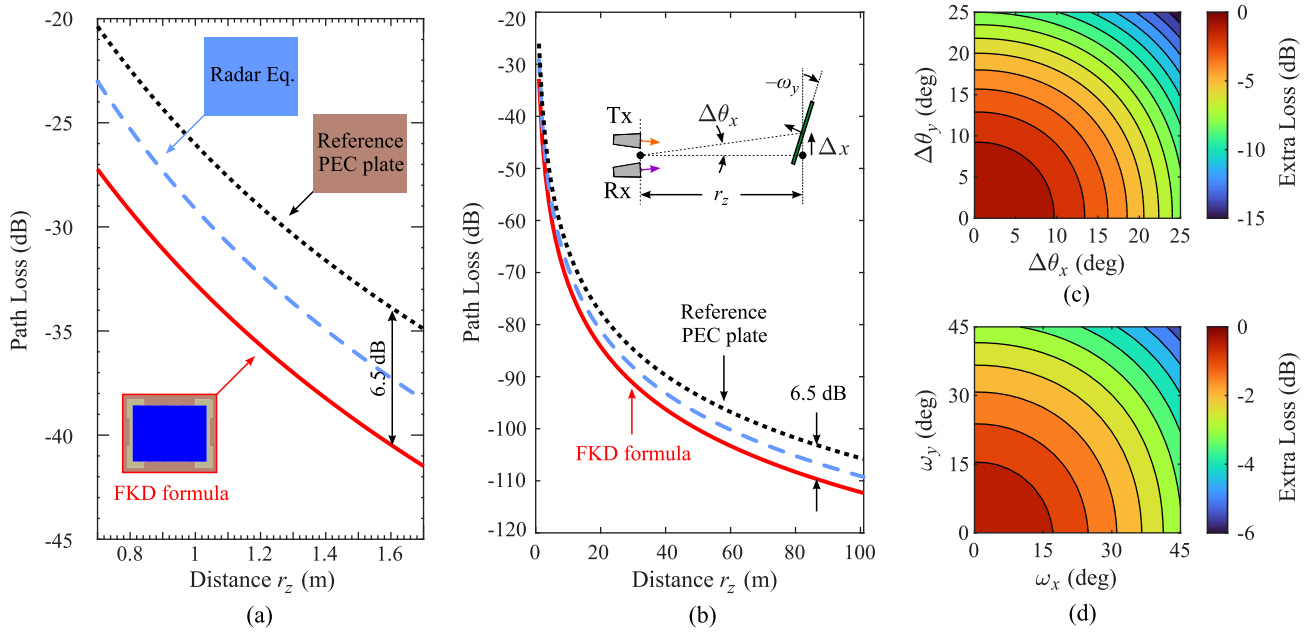
**FIGURE 6.** FKD formula-computed path loss at 5.3 GHz for the setup depicted in Fig. 5, accounting for metasurface position and orientation changes. Path loss vs. distance in the (a) near-field and (b) far-field zone, for accurate Tx/Rx-metasurface targeting, $\Delta\theta_x = 0$, and ideal metasurface orientation, $\omega_{xy} = 0$. Extra loss when (c) only a lateral space-shift $\Delta\theta_{xy}$ or (d) only a rotation $\omega_{xy}$ is applied to the metasurface, with reference to ~ 33 dB path loss at $r_z = 1$ m.
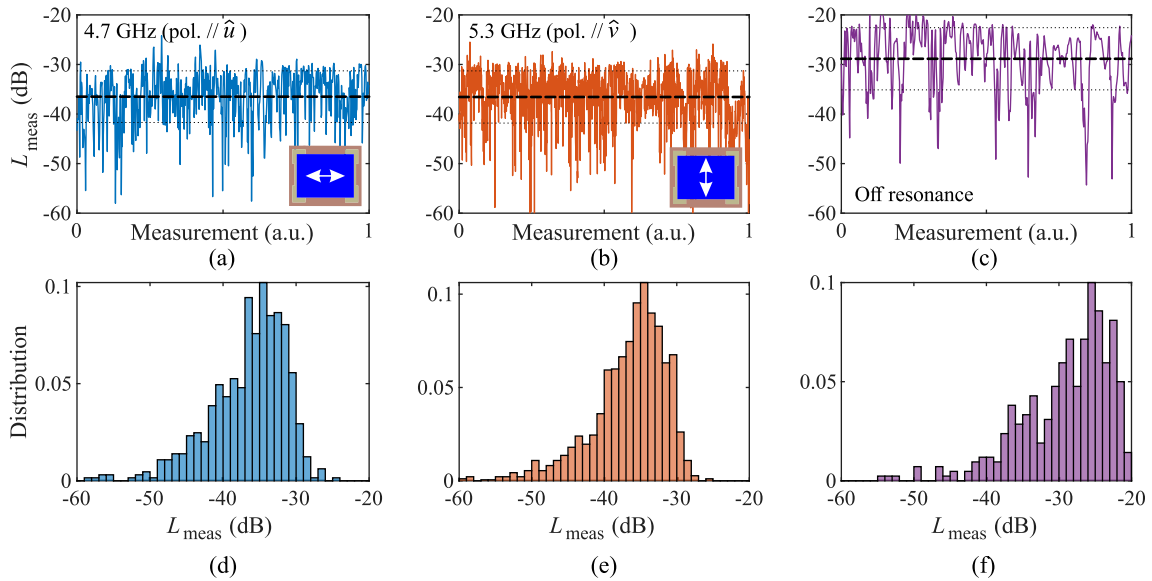


**FIGURE 7.** Top row, path loss measurements acquired during UAV flight; bottom row, corresponding histograms. Measurement on (a,d) 4.7 GHz and (b,e) 5.3 GHz absorption resonances, with antennas polarized along the long and short side of the metasurface board, respectively. (c,f) Off-resonance measurement, where the board is reflective.

each tilting, i.e., each point in Fig. 6(d), is assumed constant during the flight; however, in a real-world scenario, mechanical servo-motors mounted on the UAV could change the forward/backward tilt of the metasurface also during flight (sideways tilt is equivalent to the yaw of the UAV). From the results in Fig. 6(d), where contour lines are at 0.5 dB intervals, we observe that these absorbing metasurface boards have a very high 3 dB rotation-tolerance in excess of 40°.

The reason for this is that, even though the cells absorb less at such highly-oblique incidence angles (refer to oblique spectra in Fig. 4), the obliqueness itself means that very little power is back-scattered to the Rx antenna in this monostatic setup.

## C. EXPERIMENTAL RESULTS AND DISCUSSION
The anechoic chamber measurement setup corresponding to the schematic of Fig. 5(a) consisted of two static pyramidal

horn antennas (ATM nominal 10 dB gain at $3.95 - 5.85$ GHz, model #187-440-6) pointed at a distance of $r_z = 1$ m perpendicular to the plane defined from their apertures, where the metasurface should be placed; in a realistic PWE scenario, this could be the location indicated by the UAV orcherstrator. The path loss is measured by the $|S_{21}|$ scattering parameter recorded via a vector network analyzer (VNA, Anritsu 37397D) in CW mode.

The metasurface board was mounted on the UAV at an approximately vertical/upright orientation, as in Fig. 5(c). Subsequently, the UAV was manually flown as close as possible to the point where the antennas were targeted, $(x, y, z) = (0, 0, r_z)$ and we measured the mobility-induced fluctuations of the path loss. The measured time-series for three configurations are depicted in Figs. 7(a), 7(b), and 7(c). The first two configurations, Figs. 7(a) and 7(b), correspond to the resonances at the two frequencies identified in [28] and also simulated in Fig. 4, i.e., near 4.7 and 5.3 GHz, when the horns are polarized along the $\hat{u}$ and $\hat{v}$ directions, respectively, with reference to Fig. 2. The third configuration in Fig. 7(c) corresponds to an off-resonance frequency where the metasurface board behaves as a near-perfect reflector.

From the histograms extracted from these measurements, illustrated in Figs. 7(d), 7(e), and 7(f), we retrieve a median path loss value of $-36.5$ dB almost identical for the setups in Figs. 7(a) and 7(b), and $-29$ dB for the reference reflector setup in Fig. 7(c). There results are in line with the FKD formula predictions for $r_z = 1.2$ m, which are $-35.5$ and $-29$ dB, respectively. Note that this distance is longer than the target UAV-hover position of $r_z = 1$ m; the agreement between model and measurement would be satisfied for a 5-10 dB deeper resonance in Fig. 4. The standard deviations extracted from the histograms, approximately $\pm 5$ dB in all three cases, are in line with the FKD model predictions for the deviations of the manually-flown UAV (approximately $|\delta r_z| < 0.3$ m, $\Delta\theta < 20°$, and $\omega < 10°$) with reference to Fig. 6.

An interesting feature arising from all measurements is the asymmetry in the measured path loss distribution, with 'tails' trailing towards lower $L_{\mathrm{meas}}$ in all cases, i.e., in Figs. 7(d), 7(e), and 7(f). This feature can be attributed to two reasons: Firstly, the manually-flown UAV was instinctively moved farther from the antennas to avoid damage, secondly, the static measurements we performed indicated that this absorbing metasurface was characterized by sharp and deep absorption resonances not expected from the unit cell level simulations, as observed in Fig. 4(a) and Fig. 4(b). This latter feature, observed also in the static metasurface setup, means that a 1-2° change in the incidence direction could lead to changes of over 10 dB to measured $|S_{21}|$. This behavior, also witnessed in [28], is relevant only for near field measurements and is most likely related to the metasurface physics in this particular topology, e.g., backplane-penetrating through vias, and more generally to evanescent coupling between adjacent cells and to the finite extent of the metasurface.

## V. CONCLUSION

This paper focused on the theoretical modeling and experimental evaluation of UAV-mounted metasurface absorbers for wireless communication applications. The study utilized PO to develop a path loss model, incorporating the derivation of a transparency function to establish the connection between the incident and scattered fields. By leveraging the capabilities of PO, the diffraction phenomena in abstractly profiled metasurfaces were successfully modeled, providing valuable insights into their functionality and performance. Emphasis was given to mobility effects, by properly incorporating in our model the relative positioning and orientation of Tx/Rx antennas and metasurface aperture. The experimental measurements conducted using a state-of-the-art static absorbing metasurface and a commercial UAV validated the theoretical model, demonstrating excellent agreement between theory and experiment. Finally, our work also highlighted the importance of considering factors such as pointing accuracy, misalignment, and UAV flying stability in metasurface-assisted wireless communication scenarios.

## REFERENCES

[1] S. B. Glybovski, S. A. Tretyakov, P. A. Belov, Y. S. Kivshar, and C. R. Simovski, "Metasurfaces: From microwaves to visible," *Phys. Rep.*, vol. 634, pp. 1–72, May 2016.

[2] A. Pitilakis, O. Tsilipakos, F. Liu, K. M. Kossifos, A. C. Tasolamprou, D.-H. Kwon, M. S. Mirmoosa, D. Manessis, N. V. Kantartzis, C. Liaskos, M. A. Antoniades, J. Georgiou, C. M. Soukoulis, M. Kafesaki, and S. A. Tretyakov, "A multi-functional reconfigurable metasurface: Electromagnetic design accounting for fabrication aspects," *IEEE Trans. Antennas Propag.*, vol. 69, no. 3, pp. 1440–1454, Mar. 2021, doi: 10.1109/tap.2020.3016479.

[3] C. Liaskos, S. Nie, A. Tsioliaridou, A. Pitsillides, S. Ioannidis, and I. Akyildiz, "A new wireless communication paradigm through software-controlled metasurfaces," *IEEE Commun. Mag.*, vol. 56, no. 9, pp. 162–169, Sep. 2018.

[4] S. I. Raptis and T. V. Yioultsis, "Synthesis of polarization-independent perfect anomalous reflectors via modulated metasurfaces and an analytical design model," *IEEE Trans. Microw. Theory Techn.*, early access, May 23, 2023, doi: 10.1109/TMTT.2023.3275646.

[5] J. Ye, J. Qiao, A. Kammoun, and M.-S. Alouini, "Nonterrestrial communications assisted by reconfigurable intelligent surfaces," *Proc. IEEE*, vol. 110, no. 9, pp. 1423–1465, Sep. 2022.

[6] B. Shang, R. Shafin, and L. Liu, "UAV swarm-enabled aerial reconfigurable intelligent surface (SARIS)," *IEEE Wireless Commun.*, vol. 28, no. 5, pp. 156–163, Oct. 2021.

[7] H. Lu, Y. Zeng, S. Jin, and R. Zhang, "Aerial intelligent reflecting surface: Joint placement and passive beamforming design with 3D beam flattening," *IEEE Trans. Wireless Commun.*, vol. 20, no. 7, pp. 4128–4143, Jul. 2021.

[8] D. Tyrovolas, P.-V. Mekikis, S. A. Tegos, P. D. Diamantoulakis, C. K. Liaskos, and G. K. Karagiannidis, "On the performance of HARQ in IoT networking with UAV-mounted reconfigurable intelligent surfaces," in *Proc. IEEE 95th Veh. Technol. Conf. (VTC-Spring)*, Jun. 2022, pp. 1–5.

[9] Y. Li, C. Yin, T. Do-Duy, A. Masaracchia, and T. Q. Duong, "Aerial reconfigurable intelligent surface-enabled URLLC UAV systems," *IEEE Access*, vol. 9, pp. 140248–140257, 2021.

[10] E. M. Mohamed, S. Hashima, and K. Hatano, "Energy aware multiarmed bandit for millimeter wave-based UAV mounted RIS networks," *IEEE Wireless Commun. Lett.*, vol. 11, no. 6, pp. 1293–1297, Jun. 2022.

[11] Y. Xiao, D. Tyrovolas, S. A. Tegos, P. D. Diamantoulakis, Z. Ma, L. Hao, and G. K. Karagiannidis, "Solar powered UAV-mounted RIS networks," *IEEE Commun. Lett.*, vol. 27, no. 6, pp. 1565–1569, 2023.

[12] K. K. Nguyen, A. Masaracchia, V. Sharma, H. V. Poor, and T. Q. Duong, "RIS-assisted UAV communications for IoT with wireless power transfer using deep reinforcement learning," *IEEE J. Sel. Topics Signal Process.*, vol. 16, no. 5, pp. 1086–1096, Aug. 2022.

[13] D. Tyrovolas, P.-V. Mekikis, S. A. Tegos, P. D. Diamantoulakis, C. K. Liaskos, and G. K. Karagiannidis, "Energy-aware design of UAV-mounted RIS networks for IoT data collection," *IEEE Trans. Commun.*, vol. 71, no. 2, pp. 1168–1178, Feb. 2023.

[14] M. Sherman, S. Shao, X. Sun, and J. Zheng, "Optimizing AoI in UAV-RIS assisted IoT networks: Off policy vs. on policy," *IEEE Internet Things J.*, vol. 10, no. 14, pp. 12401–12415, Jul. 2023.

[15] S. Solanki, J. Park, and I. Lee, "On the performance of IRS-aided UAV networks with NOMA," *IEEE Trans. Veh. Technol.*, vol. 71, no. 8, pp. 9038–9043, Aug. 2022.

[16] S. K. Singh, K. Agrawal, K. Singh, C.-P. Li, and Z. Ding, "NOMA enhanced hybrid RIS-UAV-assisted full-duplex communication system with imperfect SIC and CSI," *IEEE Trans. Commun.*, vol. 70, no. 11, pp. 7609–7627, Nov. 2022.

[17] D. Wang, Y. Zhao, Y. Lou, L. Pang, Y. He, and D. Zhang, "Secure NOMA based RIS-UAV networks: Passive beamforming and location optimization," in *Proc. IEEE Global Commun. Conf. (GLOBECOM)*, Dec. 2022, pp. 3168–3173.

[18] Y. Yao, K. Lv, S. Huang, X. Li, and W. Xiang, "UAV trajectory and energy efficiency optimization in RIS-assisted multi-user air-to-ground communications networks," *Drones*, vol. 7, no. 4, p. 272, Apr. 2023. [Online]. Available: https://www.mdpi.com/2504-446X/7/4/272

[19] S. K. Singh, K. Agrawal, K. Singh, B. Clerckx, and C.-P. Li, "RSMA for hybrid RIS-UAV-aided full-duplex communications with finite blocklength codes under imperfect SIC," *IEEE Trans. Wireless Commun.*, early access, Jan. 27, 2023, doi: 10.1109/TWC.2023.3238808.

[20] C. Liaskos, S. Nie, A. Tsioliaridou, A. Pitsillides, S. Ioannidis, and I. Akyildiz, "A novel communication paradigm for high capacity and security via programmable indoor wireless environments in next generation wireless systems," *Ad Hoc Netw.*, vol. 87, pp. 1–16, May 2019. [Online]. Available: https://www.sciencedirect.com/science/article/pii/S1570870518308084

[21] D. Tyrovolas, S. A. Tegos, V. K. Papanikolaou, Y. Xiao, P.-V. Mekikis, P. D. Diamantoulakis, S. Ioannidis, C. K. Liaskos, and G. K. Karagiannidis, "Zero-energy reconfigurable intelligent surfaces (zeRIS)," 2023, *arXiv:2305.07686*.

[22] E. Basar, "Reconfigurable intelligent surfaces for Doppler effect and multipath fading mitigation," *Frontiers Commun. Netw.*, vol. 2, May 2021, Art. no. 672857.

[23] S. Jang, Y. Kim, and J. Lee, "Elimination of interference and cross talk from a face-to-face-antennas system by a metasurface absorber," *Microw. Opt. Technol. Lett.*, vol. 65, no. 9, pp. 2581–2587, Sep. 2023.

[24] P.-V. Mekikis, D. Tyrovolas, S. Tegos, A. Papadopoulos, A. Pitilakis, S. Ioannidis, A. Tsioliaridou, P. Diamantoulakis, N. Kantartzis, G. Karagiannidis, and C. Liaskos, "Dynamic programmable wireless environment with UAV-mounted static metasurfaces," in *Proc. IEEE Conf. Standards Commun. Netw. (CSCN)*, Nov. 2022, pp. 101–104.

[25] M. Al-Jarrah, A. Al-Dweik, E. Alsusa, Y. Iraqi, and M.-S. Alouini, "On the performance of IRS-assisted multi-layer UAV communications with imperfect phase compensation," *IEEE Trans. Commun.*, vol. 69, no. 12, pp. 8551–8568, Dec. 2021.

[26] P.-V. Mekikis and A. Antonopoulos, "Breaking the boundaries of aerial networks with charging stations," in *Proc. IEEE Int. Conf. Commun. (ICC)*, May 2019, pp. 1–6.

[27] S. Keşir, S. Kayraklık, I. Hökelek, A. E. Pusane, E. Basar, and A. Görçin, "Measurement-based characterization of physical layer security for RIS-assisted wireless systems," 2022, *arXiv:2212.07254*.

[28] A. Pitilakis, M. Seckel, A. C. Tasolamprou, F. Liu, A. Deltsidis, D. Manessis, A. Ostmann, N. V. Kantartzis, C. Liaskos, C. M. Soukoulis, S. A. Tretyakov, M. Kafesaki, and O. Tsilipakos, "Multifunctional metasurface architecture for amplitude, polarization and wave-front control," *Phys. Rev. Appl.*, vol. 17, no. 6, Jun. 2022, Art. no. 064060.

[29] H. Taghvaee, A. Pitilakis, O. Tsilipakos, A. C. Tasolamprou, N. V. Kantartzis, M. Kafesaki, A. Cabellos-Aparicio, E. Alarcón, and S. Abadal, "Multiwideband terahertz communications via tunable graphene-based metasurfaces in 6G networks: Graphene enables ultimate multiwideband THz wavefront control," *IEEE Veh. Technol. Mag.*, vol. 17, no. 2, pp. 16–25, Jun. 2022, doi: 10.1109/mvt.2022.3155905.

[30] F. H. Danufane, M. D. Renzo, J. de Rosny, and S. Tretyakov, "On the path-loss of reconfigurable intelligent surfaces: An approach based on Green's theorem applied to vector fields," *IEEE Trans. Commun.*, vol. 69, no. 8, pp. 5573–5592, Aug. 2021, doi: 10.1109/tcomm.2021.3081452.

[31] C. A. Balanis, *Antenna Theory*, 4th ed. Hoboken, NJ, USA: Wiley, 2016.

[32] M. Di Renzo, A. Zappone, M. Debbah, M.-S. Alouini, C. Yuen, J. de Rosny, and S. Tretyakov, "Smart radio environments empowered by reconfigurable intelligent surfaces: How it works, state of research, and the road ahead," *IEEE J. Sel. Areas Commun.*, vol. 38, no. 11, pp. 2450–2525, Nov. 2020.

[33] J. W. Goodman, *Introduction to Fourier Optics*, 2nd ed. London, U.K.: McGraw-Hill, 1996.

[34] D. F. Sievenpiper, J. H. Schaffner, H. J. Song, R. Y. Loo, and G. Tangonan, "Two-dimensional beam steering using an electrically tunable impedance surface," *IEEE Trans. Antennas Propag.*, vol. 51, no. 10, pp. 2713–2722, Oct. 2003.

[35] F. Liu, D.-H. Kwon, and S. Tretyakov, "Reflectarrays and metasurface reflectors as diffraction gratings: A tutorial," *IEEE Antennas Propag. Mag.*, vol. 65, no. 3, pp. 21–32, Feb. 2023.

[36] C.-T. Tai, *Dyadic Green Functions in Electromagnetic Theory*, 2nd ed. Piscataway, NJ, USA: IEEE Press, 1994.

[37] O. Luukkonen, C. Simovski, G. Granet, G. Goussetis, D. Lioubtchenko, A. V. Raisanen, and S. A. Tretyakov, "Simple and accurate analytical model of planar grids and high-impedance surfaces comprising metal strips or patches," *IEEE Trans. Antennas Propag.*, vol. 56, no. 6, pp. 1624–1632, Jun. 2008.

[38] D. Tyrovolas, S. A. Tegos, E. C. Dimitriadou-Panidou, P. D. Diamantoulakis, C. K. Liaskos, and G. K. Karagiannidis, "Performance analysis of cascaded reconfigurable intelligent surface networks," *IEEE Wireless Commun. Lett.*, vol. 11, no. 9, pp. 1855–1859, Sep. 2022.

[39] L. Li, T. J. Cui, W. Ji, S. Liu, J. Ding, X. Wan, Y. B. Li, M. Jiang, C.-W. Qiu, and S. Zhang, "Electromagnetic reprogrammable coding-metasurface holograms," *Nature Commun.*, vol. 8, no. 1, p. 197, Aug. 2017, doi: 10.1038/s41467-017-00164-9.

**ALEXANDROS PITILAKIS** (Senior Member, IEEE) received the Diploma degree in electrical engineering from the School of Electrical and Computer Engineering, Aristotle University of Thessaloniki (AUTH), Greece, in 2005, the M.Sc. degree in electrical engineering from ENST (Telecom) Paris, in 2007, and the Ph.D. degree in electrical engineering from the School of Electrical and Computer Engineering, AUTH, in 2013. He did an internship with the Alcatel-Lucent Optical Transmission Systems Group, Marcoussis, France. He is currently a Postdoctoral Researcher with AUTH, affiliated with the Foundation for Research and Technology Hellas (FORTH), and teaches undergraduate optics, photonics, and antennas and propagation courses with the University of Western Macedonia. His research interests include theoretical and computational electromagnetics, waveguides, antennas and propagation (optical, THz, RF), metamaterials, nonlinear optics, integrated photonics, plasmonics, and graphene. He is a member of Optica.

**DIMITRIOS TYROVOLAS** (Graduate Student Member, IEEE) received the Diploma degree in electrical and computer engineering from the University of Patras, Greece, in 2020. He is currently pursuing the Ph.D. degree with the Department of Electrical and Computer Engineering, Aristotle University of Thessaloniki, Greece. He is also a Research Assistant with the Technical University of Crete, Greece. His current research interests include reconfigurable intelligent surfaces, UAV communications, the Internet of Things networks, and probability theory. He was an exemplary Reviewer of IEEE WIRELESS COMMUNICATIONS LETTERS, in 2021, and IEEE COMMUNICATIONS LETTERS, in 2022 (top 3% of reviewers).

**PRODROMOS-VASILEIOS MEKIKIS** (Member, IEEE) received the degree in electrical and computer engineering from the Aristotle University of Thessaloniki (AUTH), in 2010, the M.Sc. degree in system-on chip design from the Royal Institute of Technology (KTH), in 2012, and the Ph.D. degree from the Technical University of Catalonia (UPC), in 2017. He is currently an Individual Marie Curie Fellow for the H2020 HERMES Project, AUTH. His research interests include UAV-based networking, network function virtualization, wireless energy harvesting, and the connectivity in massive Internet of Things networks.

**SOTIRIS A. TEGOS** (Member, IEEE) received the Diploma and Ph.D. degrees from the Department of Electrical and Computer Engineering, Aristotle University of Thessaloniki, Thessaloniki, Greece, in 2017 and 2022, respectively. In 2018, he was a Visiting Researcher with the Department of Electrical and Computer Engineering, Khalifa University, Abu Dhabi, United Arab Emirates. His research interests include wireless power transfer, probability theory, and multiple access in wireless communications. He is currently a member of the Wireless Communications and Information Processing (WCIP) group at the Aristotle University of Thessaloniki. He was an exemplary Reviewer of IEEE WIRELESS COMMUNICATIONS LETTERS, in 2019 and 2022 (top 3% of reviewers).

**ALEXANDROS PAPADOPOULOS** received the Diploma degree in electrical engineering from the Aristotle University of Thessaloniki (AUTH), Thessaloniki, Greece, in 2019. He is currently pursuing the Ph.D. degree with the Department of Computer Science and Engineering, University of Ioannina, Ioannina, Greece. Since 2020, he has been a Research Assistant with the Center for Research and Technology Hellas/Informatics and Telematics Institute (CERTH/ITI), Thessaloniki. His research interests include 5G and beyond communication networks, V2X ecosystems, metasurfaces, and wireless channel engineering.

**AGELIKI TSIOLIARIDOU** received the Diploma and Ph.D. degrees in electrical and computer engineering from the Democritus University of Thrace (DUTH), Greece, in 2004 and 2010, respectively. She is currently a Researcher with the Foundation of Research and Technology Hellas (FORTH). Her research interests include nanonetworks, with specific focus on architecture, protocols, and security/authorization issues. She has contributed to a number of EU, ESA, and national research projects.

**ODYSSEAS TSILIPAKOS** (Senior Member, IEEE) received the Ph.D. degree from the School of Electrical and Computer Engineering, Aristotle University of Thessaloniki (AUTH), in 2013. From 2014 to 2015, he was a Postdoctoral Research Fellow with AUTH. From 2016 to 2022, he was a Postdoctoral Fellow with the Institute of Electronic Structure and Laser, Foundation for Research and Technology Hellas. Since October 2022, he has been an elected Associate Researcher with the Theoretical and Physical Chemistry Institute, National Hellenic Research Foundation. His research interests include metasurfaces and metamaterials, plasmonics and nanophotonics, nonlinear optics in resonant and waveguiding structures, graphene and 2D photonic materials, and theoretical and computational electromagnetics. He is a member of Optica.

**DIONYSIOS MANESSIS** received the M.Sc. and Ph.D. degrees in materials science and engineering from the Stevens Institute of Technology, NJ, USA, and the Project Leadership Certificate degrees from Cornell University, NY, USA. He was a Technologist with Universal Instruments Corporation, NY, USA. Since 2001, he has been a Senior Technology Scientist with Fraunhofer IZM, Berlin. His research interests include fine-pitch flip-chip and wafer-level CSP bumping, solder balling, materials selection for advanced packaging technologies, the embedding processes for heterogeneous integration of components in PCBs and optical PCBs, and large scale prototype manufacturing. In the above technical fields, he has published extensively in international conferences and peer-reviewed journals.

**SOTIRIS IOANNIDIS** received the B.Sc. degree in mathematics and the M.Sc. degree in computer science from the University of Crete, in 1994 and 1996, respectively, and the Ph.D. degree from the University of Pennsylvania, in 2005. He was the Research Director of the Foundation of Research and Technology Hellas (FORTH), until 2020. He is currently an Associate Professor with the Technical University of Crete (TUC) and the Director of the Microprocessor and Hardware Laboratory.

**NIKOLAOS V. KANTARTZIS** (Senior Member, IEEE) received the Diploma and Ph.D. degrees from the Aristotle University of Thessaloniki (AUTH), Greece, in 1994 and 1999, respectively. He is currently a Professor in computational electromagnetics and electromagnetic compatibility with the School of Electrical and Computer Engineering, AUTH. He has authored/coauthored three books, nine book chapters, more than 135 peer-reviewed journal articles and 230 conference papers. His research interests include computational electromagnetics, metamaterials, graphene, real-world EMC/EMI problems, microwaves and antennas, and nanotechnology devices. He is a Senior Member of an ICS and a member of ACES.

**CHRISTOS K. LIASKOS** (Member, IEEE) received the Diploma degree in electrical engineering from the Aristotle University of Thessaloniki (AUTH), Greece, in 2004, the M.Sc. degree in medical informatics from the Medical School, AUTH, in 2008, and the Ph.D. degree in computer networking from the Department of Informatics, AUTH, in 2014. He is currently an Assistant Professor with the University of Ioannina, Ioannina, Greece, and an Affiliated Researcher with the Foundation for Research and Technology Hellas (FORTH), Heraklion, Greece. His research interests include computer networks, traffic engineering, and novel control schemes for wireless communications.

• • •

**IAN F. AKYILDIZ** (Life Fellow, IEEE) received the B.S., M.S., and Ph.D. degrees in electrical and computer engineering from the University of Erlangenrnberg, Germany, in 1978, 1981, and 1984, respectively. He has been the Founder and the President of Truva Inc., a consulting company based in Alpharetta, GA, USA, since 1989. He has been an Adjunct Professor with the University of Iceland, since 2020; the University of Helsinki, since 2021, and the University of Cyprus, since 2017. His current research interests include terahertz band communication, 6G/7G wireless systems, reconfigurable intelligent surfaces, hologram communication, extended reality wireless communications, the Internet of Space Things/CUBESATs, the Internet of Bio-Nano Things, molecular communications, and underwater and underground communications. He has been an Advisory Board Member of the Technology Innovation Institute (TII), Abu Dhabi, United Arab Emirates, since June 2020. He has also been the Founder and the Editor-in-Chief of the newly established of *International Telecommunication Union Journal on Future and Evolving Technologies* (ITU J-FET), since August 2020. He has served as the Ken Byers Chair Professor of Telecommunications, the Past Chair of the Telecom Group at the ECE, and the Director of the Broadband Wireless Networking Laboratory, Georgia Institute of Technology, from 1985 to 2020. He had many international affiliations during his career and established research centers in Spain, South Africa, Finland, Saudi Arabia, Germany, Russia, and India. He has been an ACM Fellow, since 1997. He received numerous awards from IEEE, ACM, and other professional organizations, including Humboldt Award from Germany and TUBITAK Award from Turkey.